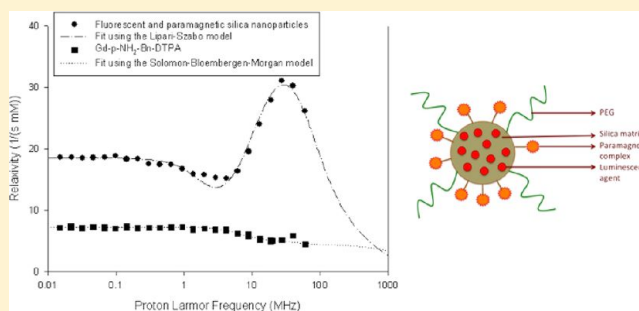


High-Relaxivity and Luminescent Silica Nanoparticles As Multimodal Agents for Molecular Imaging

Estelle Lipani,[†] Sophie Laurent,[†] Mathieu Surin,^{‡,§} Luce Vander Elst,[†] Philippe Leclère,^{‡,§} and Robert N. Muller^{*,†,||}[†]Department of General, Organic and Biomedical Chemistry, NMR and Molecular Imaging Laboratory, [‡]Laboratory for Chemistry of Novel Materials, and [§]Center of Innovation and Research in Materials and Polymers (CIRMAP), University of Mons, Place du Parc 23, 7000 Mons (BE), Belgium^{||}Center for Microscopy and Molecular Imaging (CMMI), Rue Adrienne Bolland, 8, B-6041 Gosselies, Belgium

S Supporting Information

ABSTRACT: The design and synthesis of a new bimodal contrast agent for magnetic resonance imaging and optical imaging is reported. Tunable-sized silica nanoparticles were synthesized by a microemulsion-mediated pathway and used as carriers for paramagnetic and luminescent probes. The near-infrared luminescent agent was a ruthenium complex that was directly entrapped in the silica shell to provide photoluminescence enhancement and to make it highly photostable as it was protected from the surrounding environment. The paramagnetic activity came from a Gd-DTPA derivative that was grafted on the silica surface. NMRD profiles showed a strong relaxivity enhancement (increase of 432% in the r_1 value at 20 MHz) when the paramagnetic complex was grafted at the nanoparticle surface, because of a reduction of its mobility. Polyethylene glycol was also grafted at the nanoparticle surface to enhance the nanoparticle residence time in the bloodstream. A thorough characterization of the material confirmed its potential as a very effective bimodal contrast agent.



■ INTRODUCTION

Medical imaging is the key center for the diagnosis and treatment of pathologies. Among the numerous imaging techniques, magnetic resonance imaging¹ (MRI) has become the most powerful tool for diagnosis owing to its high spatial resolution, unlimited tissue penetration, and nonionizing and noninvasive nature. Currently, most hospitals are equipped for MRI. Nevertheless, as for any imaging tool, MRI has its strengths and weaknesses. One can mention the lack of sensitivity of MRI, which is usually overcome by the administration of a contrast agent, typically gadolinium chelates.²

In an ideal medical diagnosis, defect-free images, making it possible to reveal any anatomical abnormalities precisely, are recorded with the lowest possible dose of contrast agent. Researchers are thus interested in combining imaging tools to overcome their respective limitations. The combination of MRI and optical imaging (OI), detecting the luminescence emitted by a marker, offers the high spatial resolution of the former and the high sensitivity of the latter. Such a combination of techniques is particularly useful in preclinical imaging. It has thus driven the need to create new kinds of contrast agents called multimodal contrast agents because they are active in several imaging techniques,^{3,4} where they show the same biodistribution and pharmacokinetics, unlike the situation

where two agents, each specific to one of the two techniques, are used.

Nanosized agents have captured particular attention because of their unique chemical and physical properties.⁵ They are widely used in the biomedical field, where they find applications from diagnosis to treatment. Nanosystems are being developed as labeling and tracking agents,⁶ drug carriers,^{7–9} and contrast agents.^{10–12} At the nanoscale, these objects offer considerable advantages; for example, the reduction in size results in an increase in specific surface area. Consequently, nanosystems are able to carry high payloads of vectors or reporters. In addition, because they are captured less rapidly on account of their small sizes, they show a longer lifetime in the bloodstream. This is of special interest for targeting purposes.

The interest in silica nanoparticles has recently grown because these nanoparticles are recognized as safe, biocompatible, chemically inert, and not subject to microbial attacks.^{13,14} They also appear to be valuable materials for biomedical purposes because of their high water dispersibility, the ease of their surface modification for subsequent bioconjugation, and the possibility of entrapping molecules in their cores. The chemistry of silica has also been well described.^{15–17}

Received: November 26, 2012

Revised: January 31, 2013

Published: February 5, 2013

In the present study, we report on the design of a novel nanoparticulate multimodal contrast agent active in both MRI and OI that can integrate multiple properties within one single carrier particle.¹⁸

The multimodal contrast agent reported here is based on the microemulsion-mediated synthesis of silica nanoparticles that ultimately act as a support for paramagnetic and luminescent moieties (Figure 1). A paramagnetic complex derived from the

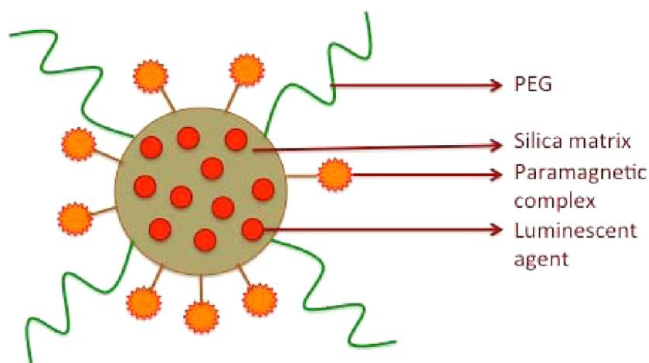


Figure 1. Structure of the bimodal agent.

well-known diethylene triamine pentaacetic acid complexed with gadolinium (Gd-DTPA) is covalently grafted to the surface of the nanoparticles. This constitutes an improvement in the relaxometry properties over previously reported nanoparticles,¹⁹ where an outer silica shell covering a gadolinium chelate reduced the water accessibility. Our DTPA derivative is substituted by an aminobenzyl group in the C4 position. It has been shown through transmetalation assessments that these derivatives are more stable and more efficient than Gd-DTPA because they exhibit a faster exchange of H₂O molecules.²⁰ As shown later, the resulting contrast agent has a high relaxivity that consequently allows for a reduction of the dose injected for an imaging session. This Gd-DTPA derivative is also more stable than those that have already been studied in the literature.^{19,21} Nanoparticles were additionally functionalized with polyethylene glycol (PEG) to extend their residence time within the body, as commonly accepted,^{22–24} by reducing the nonspecific adsorption of proteins, opsonizations, and subsequent capture by the reticulo-endothelial system.^{25–27}

To obtain activity in optical imaging, because silica nanoparticles are optically transparent, we chose to entrap a luminophore in their core. In this way, the luminophore is protected from the surrounding environment and less prone to photobleaching; consequently, its photostability is greatly increased. Moreover, the high content of dye molecules loaded per particle leads to signal enhancement.²⁸ The choice of luminophore is highly important because one of the greatest constraints limiting the use of in vivo optical imaging is tissue autofluorescence caused by endogenous fluorophores such as melanin, adipose tissue, oxyhemoglobin, and deoxyhemoglobin. To overcome this phenomenon, it is essential to work in a window where the absorption of tissues is lower, typically from 600 to 900 nm. Tris-2,2'-bipyridyl ruthenium complex meets this condition and, therefore, was entrapped in the nanoparticles during the microemulsion-mediated synthesis employed in this work.

As a whole, these silica nanoparticles will provide a highly luminescent and photostable core and a paramagnetic coating

displaying high relaxivity. This new multimodal contrast agent is therefore a good candidate for the MRI/OI combination, thus offering access to high-resolution and high-sensitivity analysis.

EXPERIMENTAL SECTION

Materials and Reagents. Tetraethoxysilane (TEOS, 99.999%), cyclohexane (>99%), Triton X-100, sodium hydroxide (NaOH) pellets, hydrochloric acid (HCl, 37%), hydrogen peroxide (H₂O₂, 35%), sodium phosphate dibasic (Na₂HPO₄), tris-(2,2'-bipyridyl)-dichlororuthenium(II) hexahydrate powder [Ru(bpy)₃Cl₂·6H₂O], ammonium hydroxide (NH₄OH), gadolinium(III) chloride hexahydrate (GdCl₃·6H₂O, 99%), and N-(3-dimethylaminopropyl)-N'-ethylcarbodiimide hydrochloride (EDCI) were purchased from Sigma-Aldrich (Bornem, Belgium). Carboxyethylsilanetriol sodium salt (CETS, 25% in water) was obtained from ABCR (Karlsruhe, Germany). 2-(4-Aminobenzyl)diethylenetriaminepentaacetic acid (p-NH₂-Bn-DTPA) was purchased from Macrocyclics (Dallas, TX). Hexanol (99%) was obtained from Acros Organics (Geel, Belgium). Methoxypolyethylene glycol amine, Chelex 100, sodium dihydrogen phosphate dihydrate (NaH₂PO₄·2H₂O,) and deionized water were purchased from Fluka (Bornem, Belgium). Nitric acid (HNO₃, 65%) was purchased from Riedel-de-Haën AG (Seelze, Germany). Finally, acetone (p.a.) and ethanol (96% p.a.) were obtained from Chem Lab (Brussels, Belgium), and centrifugal filter units (Amicon Ultra-15 10K device) were purchased from Millipore (Brussels, Belgium).

Preparation of Sorensen's Phosphate Buffer. Sorensen's phosphate buffer, consisting of disodium hydrogen phosphate and sodium dihydrogen phosphate, was the solvent used during the functionalization of silica nanoparticles. To prepare this buffer, 92 mL of sodium dihydrogen phosphate ([NaH₂PO₄] = 0.2 M) was mixed with 8 mL of disodium hydrogen phosphate ([Na₂HPO₄] = 0.2 M).

Synthesis of Luminescent Silica Nanoparticles. For each experiment, dark glassware was used to prevent photodegradation of the luminescent molecules. Luminescent silica nanoparticles were synthesized by the conventional water-in-oil microemulsion synthesis route.^{29–31} Eight milliliters of cyclohexane, 2 mL of hexanol, 2 mL of Triton X-100, and 1 mL of the luminescent solution ([Ru(bpy)₃Cl₂] = 10^{−3} M in deionized water) were mixed in a dark flask under magnetic stirring for 30 min. Subsequently, 100 μ L of TEOS was added to the flask, and the mixture was completed with the addition of 60 μ L of NH₄OH after 30 min of stirring. The reaction mixture was stirred for 24 h.

Then, 50 μ L of TEOS and 50 μ L of CETS were added with 30 min of stirring between the additions. As in the previous step, stirring was maintained for 24 h.

Finally, luminescent silica nanoparticles were precipitated with 20 mL of acetone, washed five times with ethanol, and dispersed in 5 mL of Sorensen's phosphate buffer.

Gadolinium Complexation. First, 5.4 \times 10^{−5} mol of p-NH₂-Bn-DTPA was dissolved in 1 mL of deionized water, and the pH of the solution was adjusted to 7 using sodium hydroxide. One equivalent of GdCl₃ was weighed and dissolved in 1 mL of deionized water. The gadolinium salt was slowly added to the ligand solution, and the pH of the solution was continuously adjusted between 6 and 7 with sodium hydroxide and hydrochloric acid solutions. The mixture was placed under magnetic stirring for 24 h, and the pH was frequently controlled and adjusted between 6 and 7 if needed. Finally, a small amount of Chelex 100 was added to the mixture under stirring. After 15 min, the solution was centrifuged, and the supernatant was recovered.

Surface Modification of Silica Nanoparticles. For each experiment, dark glassware was used.

Paramagnetic Coating of Silica Nanoparticles. Synthesized silica nanoparticles were placed under stirring with the paramagnetic complex. Then, 3.5 \times 10^{−4} mol of EDCI was dissolved in 1 mL of Sorensen's phosphate buffer and added to the suspension of nanoparticles. The reaction mixture was stirred for 4 h. Subsequently, the mixture was purified and washed with deionized water. Finally, the volume was reduced to 2 mL using centrifugal filter devices.

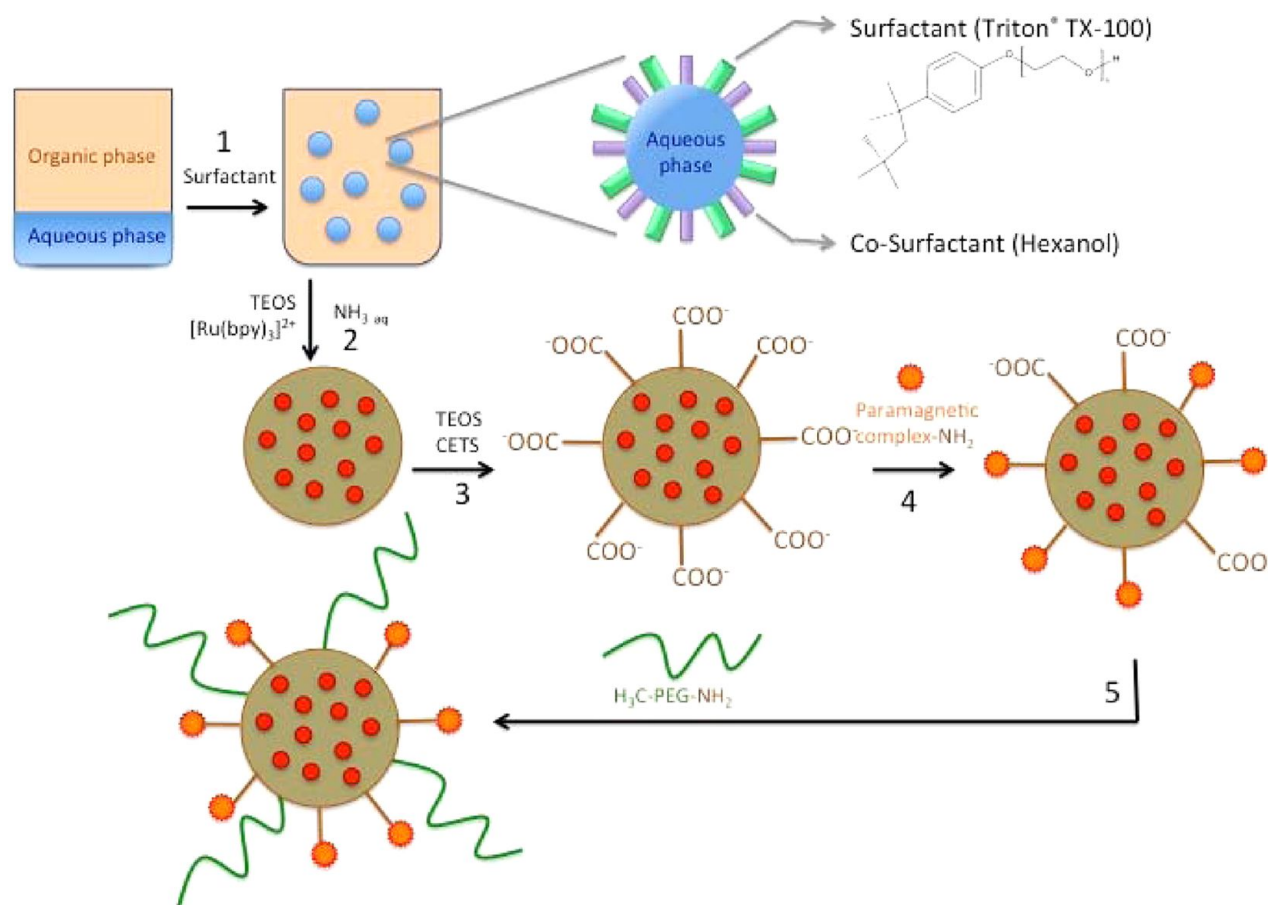


Figure 2. Synthetic route to the bimodal agent: Step 1, spontaneous formation of the microemulsion; step 2, synthesis of dye-doped silica nanoparticles; step 3, condensation of CETS on nanoparticle surface; step 4, grafting of the paramagnetic complex; step 5, grafting of the PEG.

PEGylation of Silica Nanoparticles. Methoxypolyethylene glycol amine was grafted onto the surface of silica nanoparticles by the following method.

The volume of the solution containing paramagnetic nanoparticles was completed to 5 mL with Sorensen's phosphate buffer. Then, 2.16×10^{-5} mol of methoxypolyethylene glycol amine (750) was dissolved in 2 mL of Sorensen's phosphate buffer and placed under magnetic stirring with the paramagnetic solution. Next, 3.5×10^{-4} mol of EDCI was dissolved in 1 mL of Sorensen's phosphate buffer and added to the suspension. The reaction mixture was stirred for 4 h. Subsequently, the mixture was purified, washed with deionized water, and concentrated to 2 mL by centrifugal filter devices.

Determination of Gd and Si Concentrations. The Gd and Si concentrations were determined by inductively coupled plasma-atomic emission spectroscopy (ICP-AES) analysis performed on an ISA Jobin Yvon JY-38 Plus system (Horiba, Longjumeau, France). The nanoparticles were digested by chemical and physical processes: First, 300 μ L of H_2O_2 (35%) and 600 μ L of HNO_3 (65%) were added to 500 μ L of stock solution. The mixture was then subjected to microwave treatment (power ramps between 250 and 600 W) using a Milestone MLS 1200 Mega microwave laboratory station (Apeldoorn, Netherlands). The silica and gadolinium concentrations of the digested sample were finally measured by ICP spectroscopy.

Particle Characterization. Dynamic light scattering (DLS) was used to estimate the hydrodynamic diameter and size distribution of the paramagnetic-dye-doped silica nanoparticles. Measurements were performed at 20 $^\circ\text{C}$ using a Zetasizer Zen 3600 particle size analyzer (Malvern Instruments, Malvern, U.K.).

Transmission electron microscopy (TEM) analyses were performed on a Tecnai 10 microscope (FEI, Hillsboro, OR) to obtain particle sizes, size distributions, and morphologies. Samples were prepared

from aqueous dispersions of paramagnetic-dye-doped silica nanoparticles deposited on carbon-coated copper grids.

Atomic force microscopy (AFM) analyses were carried out on a Multimode III AFM system with tips (model NCHV; $k = 20\text{--}80$ N/m, $W = 30\text{--}50$ μm , $f_0 = 332\text{--}379$ kHz) from Bruker (Karlsruhe, Germany). Samples with a nanoparticle concentration of 0.1 mg/mL were deposited on freshly cleaved muscovite mica at room temperature. Images were acquired in tapping mode in air and analyzed with the NanoScope Analysis software from Bruker and WSxM 5.0 software from Nanotec Electronica (Madrid, Spain).

The zeta potential of the nanoparticles was measured using a Zetasizer Zen 3600 particle size analyzer (Malvern Instruments, Malvern, U.K.). Measurements were performed at 25 $^\circ\text{C}$ and pH 7 using a standard capillary cell. The dielectric constant was set to 78.5, and the Smoluchowski constant, $f(Ka)$, was 1.5.

Photophysical Study. The fluorescent properties of the sample were characterized through absorption and emission spectroscopies.

Absorbance spectra were collected on a Lambda 35 UV/vis spectrometer (Perkin-Elmer, Wellesley, MA), whereas emission spectra were collected on an LS55 fluorescence spectrometer (Perkin-Elmer, Wellesley, MA).

Fluorescence images were acquired using a Biospace Lab Photon Imager and M3 Vision software (Biospace Lab, Paris, France).

Measurement of Relaxivity. Data Acquisition. Longitudinal relaxation times were measured at 37 $^\circ\text{C}$ on Bruker MINISPEC mq-20 and mq-60 spin analyzers working at 20 and 60 MHz, respectively; these values were pooled in the nuclear magnetic relaxation dispersion (NMRD) profiles.

NMRD profiles were collected at 37 $^\circ\text{C}$ over a range of resonance frequencies extending from 0.01 to 40 MHz on a fast field-cycling relaxometer (Stelar, Mede, Italy).

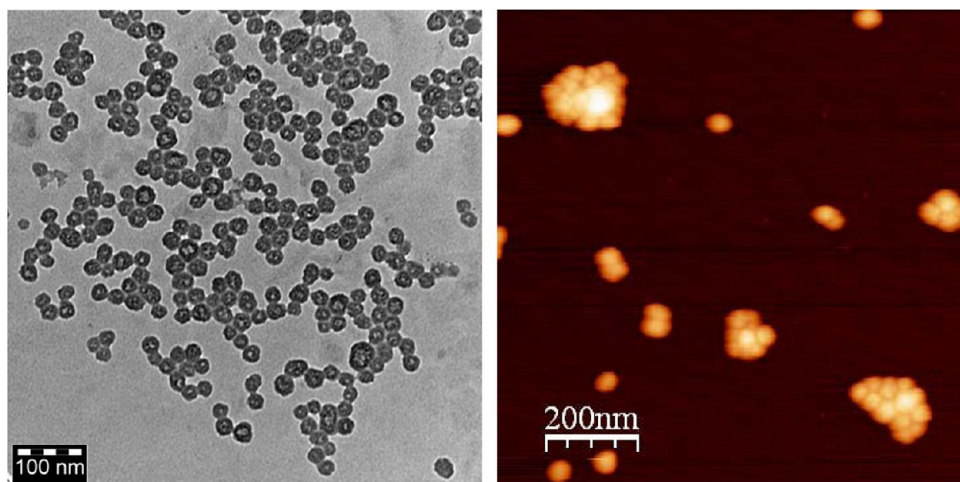


Figure 3. (a) TEM and (b) AFM images of nondoped silica nanoparticles coated with CETS (height scale is 45 nm).

Correction of the ^1H NMRD Data. As silica nanoparticles are known to contribute to the water relaxation rate at low field, uncoated luminescent silica nanoparticles with a size similar to that of our contrast agent were synthesized by means of the microemulsion process, and their NMRD profile was recorded at the same silica concentration. Their profile was fitted with the Cole–Cole model and was subtracted from the ^1H NMRD data of the paramagnetic silica nanoparticles.

Fitting of the ^1H NMRD Data. Two models were employed for the fitting of the ^1H NMRD data: the classical Solomon–Bloembergen model in the case of the Gd-DTPA derivative^{32,33} and the Lipari–Szabo model (sometimes referred to as a “model-free” approach)^{34,35} when the Gd-DTPA derivative was grafted on the surface of the silica nanoparticles.

Briefly, the Lipari–Szabo model, often used to describe the dynamics of proteins, is based on the fact that the overall rotational motion of the nanoparticle and the internal local movements have different time scales so that they can be considered as independent. The slow global motion of the entire molecule is defined by the correlation time τ_{rg} , whereas the fast local rotation (of the Gd³⁺ complex on the nanoparticle surface) is defined by τ_{rl} . This theory also involves the general order parameter S^2 , related to the degree of spatial restriction of the local motion. $S^2 = 0$ indicates that the internal motion is totally free, whereas $S^2 = 1$ indicates that the local rotational dynamics is determined only by the global motion.

It is known that the effect of a Gd chelate on the longitudinal relaxation rate of water molecules (R_1^{p}) depends on both the inner-sphere (superscript is) and outer-sphere (superscript os) mechanisms and is given by the equations³⁶

$$R_1^{\text{p}} = R_1^{\text{is}} + R_1^{\text{os}} \quad (1)$$

$$R_1^{\text{is}} = \frac{fq}{T_{1\text{M}} + \tau_{\text{M}}} \quad (2)$$

According to the Lipari–Szabo model theory, the longitudinal relaxation rate of inner-sphere protons ($1/T_{1\text{M}}$) is given by

$$\frac{1}{T_{1\text{M}}} = \frac{2}{15} \left(\frac{\mu_0}{4\pi} \right)^2 \gamma_1^2 \gamma_s^2 \hbar^2 S(S+1) \frac{1}{r_{\text{GDH}}^6} [3j(\omega_{\text{I}}, \tau_{\text{C1}}) + 7j(\omega_{\text{S}}, \tau_{\text{C2}})] \quad (3)$$

where γ_{S} and γ_{I} are the electron and nuclear gyromagnetic ratios, respectively ($\gamma_{\text{S}} = 1.76 \times 10^{11} \text{ rad s}^{-1} \text{ T}^{-1}$, $\gamma_{\text{I}} = 2.675 \times 10^8 \text{ rad s}^{-1} \text{ T}^{-1}$), and r_{GDH} is the effective distance between the electron charge and the ^1H nucleus. Finally, the spectral density functions are expressed in the equations

$$j(\omega_{\text{I}}, \tau_{\text{C1}}) = \left[\frac{S^2 \tau_{\text{C1g}}}{1 + \omega_{\text{I}}^2 \tau_{\text{C1g}}^2} + \frac{(1 - S^2) \tau_{\text{C1l}}}{1 + \omega_{\text{I}}^2 \tau_{\text{C1l}}^2} \right] \quad (4)$$

$$j(\omega_{\text{S}}, \tau_{\text{C2}}) = \left[\frac{S^2 \tau_{\text{C2g}}}{1 + \omega_{\text{S}}^2 \tau_{\text{C2g}}^2} + \frac{(1 - S^2) \tau_{\text{C2l}}}{1 + \omega_{\text{S}}^2 \tau_{\text{C2l}}^2} \right] \quad (5)$$

$$\frac{1}{\tau_{\text{Cig}}} = \frac{1}{\tau_{\text{rg}}} + \frac{1}{\tau_{\text{M}}} + \frac{1}{\tau_{\text{si}}} \quad i = 1, 2 \quad (6)$$

$$\frac{1}{\tau_{\text{Cil}}} = \frac{1}{\tau_{\text{rg}}} + \frac{1}{\tau_{\text{rl}}} + \frac{1}{\tau_{\text{M}}} + \frac{1}{\tau_{\text{si}}} \quad i = 1, 2 \quad (7)$$

where τ_{si} and τ_{sl} are the longitudinal and transverse relaxation times, respectively, of the electron; τ_{rg} is the correlation time for global motion; τ_{rl} is the correlation time for fast local motion; ω_{S} and ω_{I} are the Larmor frequencies of the electron and proton, respectively; and S is the order parameter.

MRI Image Acquisition. A T_1 -weighted MRI image of the bimodal agent was acquired at room temperature on a 7 T PharmaScan 70:16 imaging system (Bruker, Karlsruhe, Germany) using a spin–echo sequence with the rapid acquisition with relaxation enhancement (RARE) method [echo time (TE), 8.2 ms; repetition time (TR), 500 ms; slice thickness, 1 mm; matrix, 256×256].

RESULTS AND DISCUSSION

Silica nanoparticles were synthesized by the well-described water-in-oil (w/o) microemulsion process^{29–31} (Figure 2). A w/o microemulsion is defined as a thermodynamically stable solution of oil, water, and surfactant. Aqueous solution is confined in nanosized droplets distributed in a continuous domain of oil. The first step of the synthesis involves the hydrolysis of TEOS in the presence of ammonia (basic catalysis), and in the second step, silica nanoparticles are formed in the micelles by the condensation of hydrolyzed silica species while the luminophore is directly entrapped.³⁷ Then, the surface of the nanoparticles is treated with CETS,³⁸ so that the resulting nanoparticles present carboxyl groups for further functionalization.

Microemulsion-mediated synthesis offers the advantages of being conducted at room temperature and under atmospheric pressure and of producing nanoparticles with a narrow size distribution because the micelles act as nanoreactors. For biomedical applications, the latter point is of paramount importance because size is known to affect the biodistribution,

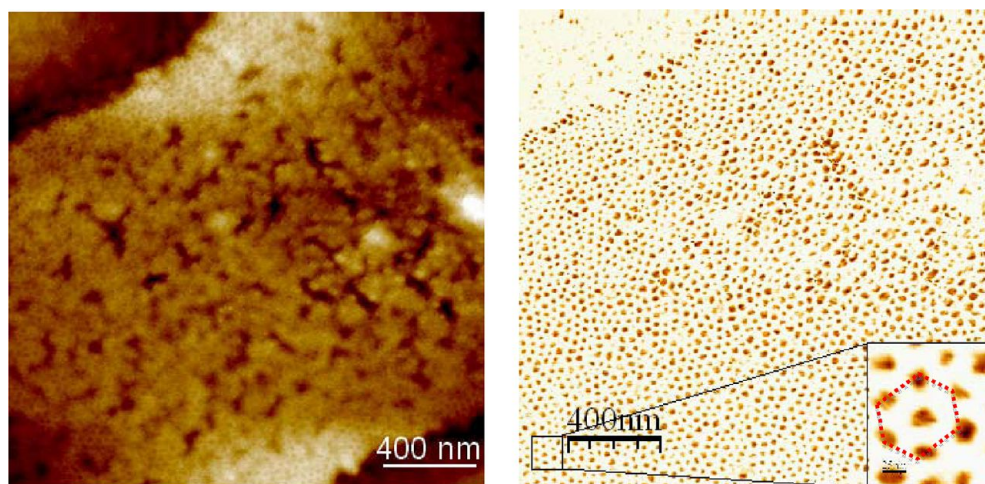


Figure 4. AFM (a) height image (height scale from 0 to 60 nm) and (b) phase image of fluorescent paramagnetic silica nanoparticles. Inset: Enlarged image showing hexagonal close-packing arrangement in this layer of nanoparticles.

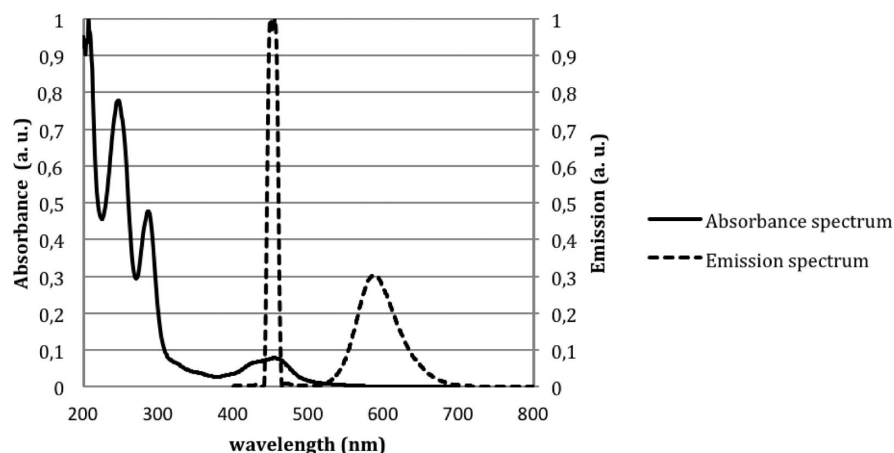


Figure 5. Absorbance and emission spectra of fluorescent and paramagnetic silica nanoparticles.

intracellular mobility, and metabolism of nanoparticles.^{39–41} Finally, this synthetic route also offers the possibility of producing controlled-size nanoparticles by tuning the micro-emulsion parameters.^{42–50} Taken together, these advantages constitute improvements over a previous study⁵¹ in which lanthanide-DTPA-grafted silica nanoparticles were synthesized by a method derived from the Stöber process.

Silica nanoparticles with carboxylic functions were finally coupled with the paramagnetic complex and PEG using EDCI.

After purification, the batch was comprehensively characterized with respect to morphology, relaxometry, and photophysical properties. The silica and gadolinium concentrations were quantified by ICP spectroscopy and were 10.65 and 1.55 mM, respectively.

Particle Characterization. Two types of silica nanoparticles were characterized: nondoped silica nanoparticles coated with CETS and fluorescent paramagnetic silica nanoparticles.

Nondoped Silica Nanoparticles Coated with CETS. The zeta potential of the nondoped silica nanoparticles coated with CETS was measured at -27.1 ± 2.6 mV at pH 7.

The size distribution of the silica nanoparticles was determined by several techniques.

Dynamic light scattering (DLS) was used to assess the hydrodynamic diameter of the nanoparticles. The results

showed that a single population was present in the sample with a mean hydrodynamic diameter (d_{hd}) of 26 ± 1 nm and a narrow size distribution.

Transmission electron microscopy (TEM) images show small, uniform, and spherical nanoparticles (Figure 3a) with a mean diameter (d) of about 26 ± 4 nm.

These results were compared to AFM measurements (Figure 3b). One can clearly distinguish small isolated nanoparticles and larger aggregates. After tip convolution was taken into account, particle analysis gave a mean diameter (d) equal to 27 ± 4 nm and a mean height equal to 28 ± 7 nm.

The diameters obtained by the different techniques are thus in excellent agreement. The TEM and AFM images both showed small, uniform, and spherical nanoparticles with a narrow size distribution.

Fluorescent Paramagnetic Silica Nanoparticles. The zeta potential of the fluorescent paramagnetic silica nanoparticles was -25.7 ± 1.9 mV at pH 7.

DLS measurements were performed before and after functionalization of the silica nanoparticles. The mean d_{hd} value before functionalization was 36 ± 3 nm, whereas that of the coated nanoparticles was 42 ± 4 nm.

The average thickness of the coating was thus around 3 nm. The AFM measurements display a locally hexagonal close-packed arrangement of uniform round-shaped objects, and one

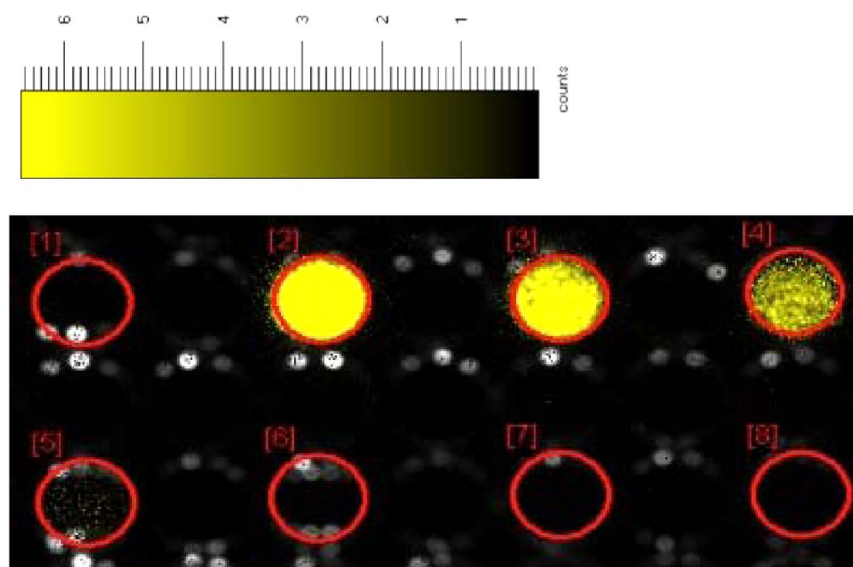


Figure 6. Optical imaging experiment performed on fluorescent paramagnetic silica nanoparticles (samples 1 and 8 correspond to water; samples 2–7 correspond to silica nanoparticles diluted 5, 10, 20, 200, 2000, and 20000 times, respectively).

can clearly observe silica nanoparticles and their coating (Figure 4a). The average diameter of the entire nanoparticle was 44 ± 4 nm.

The diameters obtained by DLS and AFM measurements were in good agreement. From the phase image (Figure 4b), one can observe that the silica core and its coating had different contrasts, which indicates that the structures of the silica core and the coating were characterized by different mechanical properties.

Photophysical Study. The choice of the fluorophore is critical for optical imaging experiments to increase tissue penetration.^{52,53} Tris-2,2'-bipyridyl ruthenium complex, a near-infrared fluorophore that seems to be a good candidate for optical imaging analysis, was chosen. Nevertheless, this complex presents a Jablonski diagram slightly different from that of organic molecules, offering a range of additional transitions.⁵⁴ Ruthenium in the 2+ oxidation state is in the d^6 configuration, and exposure of the complex to a light beam of 455-nm wavelength involves the promotion of a d electron to a ligand antibonding orbital. This is an MLCT (metal-to-ligand charge-transfer) transition, an S_0 – S_1 transition in the conventional Jablonski diagram. This results in an $^1\text{MLCT}$ – $^3\text{MLCT}$ transition that is effective because ruthenium is a heavy atom and radiative emissions occur from this state at a wavelength between 585 and 600 nm.

An absorbance spectrum was recorded on the sample ($[\text{Si}] = 1.065$ mM, $[\text{Gd}] = 0.155$ mM) (Figure 5, solid line) and was found to be similar to that of the ruthenium complex. Three absorption peaks were observed: The two high-energy peaks correspond to ligand–ligand transitions, whereas the peak of interest is located around 455 nm with a shoulder at 429 nm. These results confirm that the fluorophore was entrapped in the silica shell.

The emission spectrum of the sample ($[\text{Si}] = 106.5$ μM , $[\text{Gd}] = 15.5$ μM) (Figure 5, dashed line) shows a strong emission around 587 nm that is ideally located in the area where the absorbance of tissues consisting of water, fat, blood, and proteins is the lowest.

Optical imaging experiments were performed on the sample at different concentrations. Samples were placed in a black 96-

well plate (Figure 6) and excited at 455 nm. Positions 1 and 8 correspond to water, whereas positions 2–7 correspond to the sample at silicon concentrations of 2.13 mM ($[\text{Gd}] = 0.31$ mM), 1.065 mM ($[\text{Gd}] = 0.155$ mM), 532.5 μM ($[\text{Gd}] = 0.0775$ mM), 53.25 μM ($[\text{Gd}] = 7.75$ μM), 5.325 μM ($[\text{Gd}] = 0.775$ μM), and 0.5325 μM ($[\text{Gd}] = 0.0775$ μM), respectively.

Wells 1 and 8 contained pure water, for which no emission occurred when excited at 455 nm. A strong emission was clearly observed in wells 2–4 containing fluorescent and paramagnetic silica nanoparticles, and a weaker signal was observed in well 5. This signal was completely lost when the silicon concentration was 5.325 μM (wells 6 and 7).

Intensities [which are related to the number of counted photons per unit of time per unit of area and taking into account the spherical field view of the camera ($\text{photons s}^{-1} \text{cm}^{-2} \text{sr}^{-1}$)] are plotted as a function of concentration in Figure 7. Analyses were performed three times.

Relaxometry Study. Relaxometry studies were performed on fluorescent paramagnetic silica nanoparticles as well as on the free paramagnetic complex in solution.

NMRD profiles are shown in Figure 8. One can clearly note that the relaxivity of silica nanoparticles was, as expected for slowly tumbling systems, much higher than that of the small

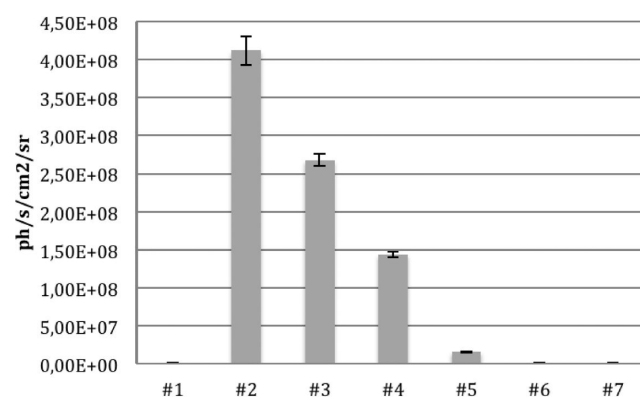


Figure 7. Signal intensities ($\text{photons s}^{-1} \text{cm}^{-2} \text{sr}^{-1}$) recorded in wells 1–7 during the optical imaging experiments.

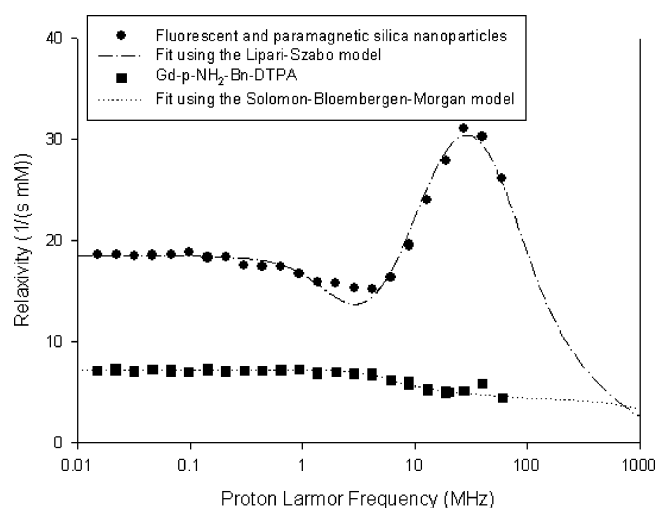


Figure 8. NMRD profiles of the paramagnetic complex grafted on silica nanoparticles and of Gd-DTPA derivative in solution. Relaxivities are reported in terms of $(\text{s mM})^{-1}$ relative to $[\text{Gd}^{3+}]$.

complex alone. The shape of the NMRD profile of the free Gd-DTPA derivative is characteristic of small paramagnetic complexes⁵⁵ and was easily fitted by the conventional Solomon–Bloembergen–Morgan model, whereas the shape of the profile of the fluorescent and paramagnetic silica nanoparticles is typical of high-molecular-weight paramagnetic species, confirming that the paramagnetic complex was indeed grafted on the surface of silica nanoparticles. Conventional paramagnetic models are not ideally suited to these kinds of high-molecular-weight species, so the NMRD profile was fitted according to the Lipari–Szabo model.^{34,35}

Specific parameters can be extracted from the fitting of the NMRD profiles (Table 1), as well as the residence time of

Table 1. Parameters Extracted from the Fitted NMRD Profiles

	free Gd-p-NH ₂ -Bn-DTPA	fluorescent paramagnetic silica nanoparticles
τ_r (ns)	0.09	$\tau_{rg} = 2.04$ $\tau_{rl} = 0.35$ $S^2 = 0.455$
τ_M^a (μs)	0.1	0.1
τ_{so} (ps)	73.6	163
τ_v (ps)	31.8	44

^aValue of τ_M fixed at 100 ns on the basis of previous estimations performed on C4 derivatives of Gd-DTPA through the measurement of the reduced transverse relaxation rate of ^{17}O at different temperatures.³⁶

water molecules coordinated to the complex (τ_M), the electronic relaxation time at very low field (τ_{so}), and the correlation time for the modulation of the zero field splitting (τ_v).

The global correlation time of the paramagnetic nanoparticles was more than 20 times longer than the rotational correlation time of the free paramagnetic complex in solution, which confirms that the paramagnetic entities were anchored on the nanoparticles. The local correlation time (τ_{rl}) was longer than the τ_r value of the free Gd-DTPA complex in solution, again confirming that the paramagnetic complex was linked to a nanosystem. No significant change in τ_v values was observed

when the complex was free or linked, whereas τ_{so} was slightly higher when the complex was grafted onto silica nanoparticles. As expected, grafting of the paramagnetic complex on the surface of the nanoparticles enhanced its relaxivity by increasing its rotational correlation time.

A T_1 -weighted image was captured to demonstrate the efficiency of the probe as an MRI contrast agent (Figure 9).

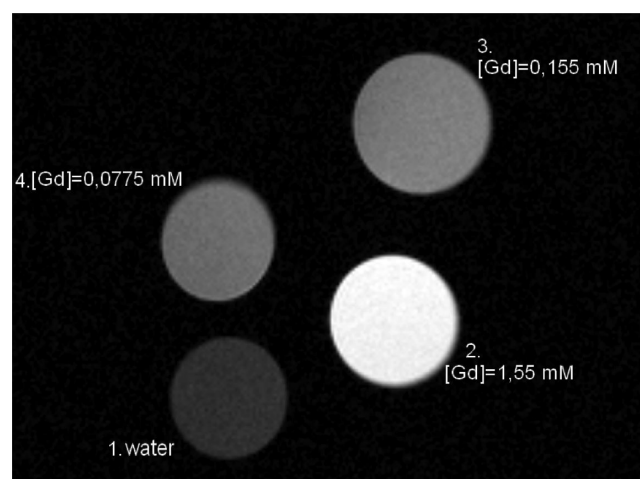


Figure 9. T_1 -weighted image of the luminescent and paramagnetic silica nanoparticles.

Compared to water, one can clearly note a positive contrast enhancement. Samples 3 and 4 in Figure 9 correspond to samples 3 and 4, respectively, in the optical image (Figure 6), which clearly demonstrates the potential of the probe in both MRI and OI techniques.

CONCLUSIONS

Multimodal paramagnetic and luminescent silica nanoparticles have been successfully synthesized by means of a micro-emulsion-based approach. This synthetic pathway makes it possible to produce, at room temperature, tunable-sized nanoparticles with a narrow size distribution. This is of great interest in biomedical applications because the size of an object is known to play a key role in its pharmacokinetic properties. The optical properties of the ruthenium complex were not compromised by the incorporation of the complex in the colorless, transparent silica matrix. Protected from the surrounding environment, this complex exhibits high photostability and strong luminescence emission in the near-infrared range; consequently, further in vivo studies should give the best tissue penetration expected for optical imaging. Grafting a paramagnetic complex derived from the well-known Gd-DTPA complex onto the surface of the nanoparticles was found to provide dramatic relaxivity enhancement mostly due to a reduction of the ligand mobility. Taken together, the characterizations we performed demonstrate that the bimodal agent is a promising candidate for the combination of MRI and OI. Moreover, this material could also find applications in computed tomography as an opaque contrast agent because of the ruthenium present in the core¹⁹ of the nanoparticle and Gd could also be used as a radiosensitizer in neutron capture therapy.⁵⁶

Further studies will encompass grafting a peptide for molecular imaging and assessing the toxicity of the bimodal contrast agent through cytotoxic assays.

■ ASSOCIATED CONTENT

■ Supporting Information

Signal intensity data from optical imaging experiments and experimental ^1H NMRD data. This material is available free of charge via the Internet at <http://pubs.acs.org>.

■ AUTHOR INFORMATION

Corresponding Author

*E-mail: robert.muller@umons.ac.be.

Notes

The authors declare no competing financial interest.

■ ACKNOWLEDGMENTS

E.L. thanks the FRIA, FNRS, ARC, and ENCITE programs for financial support. M.S. and Ph.L. are Research Associates from F.R.S.-FNRS (Belgium). The authors acknowledge the Center for Microscopy and Molecular Imaging (CMMI), supported by the European Regional Development Fund and the Walloon region. Ms. Corine Piérart, Dr. Lionel Larbanoix, and Mr. Mathieu Roch are thanked for their help in ICP measurements, optical imaging, and magnetic resonance imaging experiments, respectively.

■ REFERENCES

- (1) Rinck, P. A. *Magnetic Resonance in Medicine*; ABW Wissenschaftsverlag: Berlin, 2003.
- (2) Yan, G.-P.; Robinson, L.; Hogg, P. Magnetic resonance imaging contrast agents: Overview and perspectives. *Radiography* **2007**, *13*, e5–e19.
- (3) Frullano, L.; Meade, T. J. Multimodal MRI contrast agents. *J. Biol. Inorg. Chem.* **2007**, *12*, 939–949.
- (4) Chul Paeng, J.; Soo Lee, D. Multimodal Molecular Imaging In Vivo. *Open Nucl. Med. J.* **2010**, *2*, 145–152.
- (5) Hyuk Suh, W.; Suh, Y.-H.; Stucky, G. D. Multifunctional nanosystems at the interface of physical and life sciences. *Nano Today* **2009**, *4*, 27–36.
- (6) Boisseau, P.; Loubaton, B. Nanomedicine, nanotechnology in medicine. *C. R. Phys.* **2011**, *12*, 620–636.
- (7) Singh, R.; Lillard, J. W., Jr. Nanoparticle-based targeted delivery. *Exp. Mol. Pathol.* **2009**, *86*, 215–223.
- (8) Kidane, A.; Bhatt, P. P. Recent advances in small molecule drug delivery. *Curr. Opin. Chem. Biol.* **2005**, *9*, 347–351.
- (9) Labhasetwar, V. Nanotechnology for drug and gene therapy: The importance of understanding molecular mechanisms of delivery. *Curr. Opin. Biotechnol.* **2005**, *16*, 674–680.
- (10) Koo, O. M.; Rubinstein, I.; Onyuksel, H. Role of nanotechnology in targeted drug delivery and imaging: A concise review. *Nanomedicine: NBM* **2005**, *1*, 193–212.
- (11) Pan, D.; Lanza, G. M.; Wickline, S. A.; Caruthers, S. D. Nanomedicine: Perspective and promises with ligand-directed molecular imaging. *Eur. J. Radiol.* **2009**, *70*, 274–28.
- (12) De, M.; Chou, S. S.; Joshi, H. M.; Dravid, V. P. Hybrid magnetic nanostructures (MNS) for magnetic resonance imaging applications. *Adv. Drug Delivery Rev.* **2011**, *63*, 1282–1299.
- (13) Knopp, D.; Tang, D.; Niessner, R. Review: Bioanalytical applications of biomolecule-functionalized nanometer-sized doped silica particles. *Anal. Chim. Acta* **2009**, *647*, 14–30.
- (14) Wang, L.; Zhao, W.; Tan, W. Bioconjugated Silica Nanoparticles: Development and Applications. *Nano Res.* **2008**, *1*, 99–115.
- (15) Brinker, C. J. Hydrolysis and condensation of silicates: Effects on structure. *J. Non-Cryst. Solids* **1988**, *100*, 31–50.
- (16) Hauser, E. A. The Colloid Science of Silica and Silicones. *Clays Clay Miner.* **1955**, *4*, 45–53.
- (17) Chatterji, S. Chemistry of alkali–silica reaction and testing of aggregates. *Cem. Concr. Compos.* **2005**, *27*, 788–795.
- (18) Na, H. B.; Hyeon, T. Nanostructured T1MRI contrast agents. *J. Mater. Chem.* **2009**, *19*, 6267–6273.
- (19) Santra, S.; Bagwe, R. P.; Dutta, D.; Stanley, J. T.; Walter, G. A.; Tan, W.; Moudgil, B. M.; Mericle, R. A. Synthesis and characterisation of fluorescent, radio-opaque, and paramagnetic silica nanoparticles for multimodal bioimaging applications. *Adv. Mater.* **2005**, *17*, 2165–2169.
- (20) Laurent, S.; Botteman, F.; Vander Elst, L.; Muller, R. N. Relaxivity and Transmetalation Stability of New Benzyl-Substituted Derivatives of Gadolinium–DTPA Complexes. *Helv. Chim. Acta* **2004**, *87*, 1077–1089.
- (21) Rieter, W. J.; Kim, J. S.; Taylor, K. M. L.; An, H.; Lin, W.; Tarrant, T.; Lin, W. Hybrid silica nanoparticles for multimodal imaging. *Angew. Chem., Int. Ed.* **2007**, *46*, 3680–3682.
- (22) Michel, R.; Pasche, S.; Textor, M.; Castner, D. G. The Influence of PEG Architecture on Protein Adsorption and Conformation. *Langmuir* **2005**, *26*, 12327–12332.
- (23) Charles, P. T.; Stubbs, V. R.; Soto, C. M.; Martin, B. D.; White, B. J.; Taitt, C. R. Reduction of Non-Specific Protein Adsorption Using Poly(ethylene) Glycol (PEG) Modified Polyacrylate Hydrogels In Immunoassays for Staphylococcal Enterotoxin B Detection. *Sensors* **2009**, *9*, 645–655.
- (24) Kingshott, P.; McArthur, S.; Thissen, H.; Castner, D. G.; Griesser, H. J. Ultrasensitive probing of the protein resistance of PEG surfaces by secondary ion mass spectrometry. *Biomaterials* **2002**, *23*, 4775–4785.
- (25) Bagwe, R. P.; Hilliard, L. R.; Tan, W. Surface modification of silica nanoparticles to reduce aggregation and nonspecific binding. *Langmuir* **2006**, *22*, 4357–4362.
- (26) He, Q.; Zhang, J.; Shi, J.; Zhu, Z.; Zhang, L.; Bu, W.; Guo, L.; Chen, Y. The effect of PEGylation of mesoporous silica nanoparticles on nonspecific binding of serum proteins and cellular responses. *Biomaterials* **2010**, *31*, 1085–1092.
- (27) Cauda, V.; Schlossbauer, A.; Bein, T. Bio-degradation study of colloidal mesoporous silica nanoparticles: Effect of surface functionalization with organo-silanes and poly(ethylene glycol). *Microporous Mesoporous Mater.* **2010**, *132*, 60–71.
- (28) Kim, N.; Oh, S.-M.; Kim, C.-T.; Kim, C.-J.; Cho, Y.-J. Morphology and fluorescence properties of dye-entrapped silica nanoparticles. *Proc. Food Sci.* **2011**, *1*, 7–11.
- (29) Finnie, K. S.; Bartlett, J. R.; Barbé, C. J. A.; Kong, L. Formation of silica nanoparticles in microemulsions. *Langmuir* **2007**, *23*, 3017–3024.
- (30) Lopez-Quintela, M. A.; Tojo, C.; Blanco, M. C.; Garcia Rio, L.; Leis, J. R. Microemulsion dynamics and reactions in microemulsions. *Curr. Opin. Colloid Interface Sci.* **2004**, *9*, 264–278.
- (31) Chang, C.-L.; Fogler, H. S. Kinetics of Silica Particle Formation in Nonionic W/O Microemulsions from TEOS. *AIChE J.* **1996**, *42* (11), 3153–3163.
- (32) Solomon, I. Relaxation processes in a system of two spins. *Phys. Rev.* **1955**, *99*, 559–565.
- (33) Bloembergen, N. Proton relaxation times in paramagnetic solutions. *J. Chem. Phys.* **1957**, *27*, 572–573.
- (34) Lipari, G.; Szabo, A. Model-free approach to the interpretation of nuclear magnetic resonance relaxation in macromolecules. 1. Theory and range of validity. *J. Am. Chem. Soc.* **1982**, *104* (17), 4546–4559.
- (35) Dunand, F. A.; Toth, E.; Hollister, R.; Merbach, A. E. Lipari–Szabo approach as a tool for the analysis of macromolecular gadolinium(III)-based MRI contrast agents illustrated by the $[\text{Gd}(\text{EGTA-BA}-(\text{CH}_2)_{12})_n]^{n+}$ polymer. *J. Biol. Inorg. Chem.* **2001**, *6*, 247–255.
- (36) Laurent, S.; Henoumont, C.; Vander Elst, L.; Muller, R. N. Current Developments in Contrast Agents: Synthesis and Physico-Chemical Characterisation of Paramagnetic Contrast Agents for MRI. *Eur. J. Inorg. Chem.* **2012**, *12*, 1889–1915.
- (37) Wang, Q.; Choy, R.; Dai, Q.; Ostafin, A. E. Preparation of dye-loaded SiO_2 nanoparticles. *J. Non-Cryst. Solids* **2007**, *353*, 354–365.

- (38) Lee, C. H.; Park, S. H.; Chung, W.; J., Y.; Kim, S. H. Preparation and characterization of surface modified silica nanoparticles with organo-silane compounds. *Colloids Surf. A* **2011**, *384*, 318–322.
- (39) Fadeel, B.; Garcia-Bennett, A. E. Better safe than sorry: Understanding the toxicological properties of inorganic nanoparticles manufactured for biomedical applications. *Adv. Drug Delivery Rev.* **2010**, *62*, 362–374.
- (40) Cho, M.; Cho, W.-S.; Choi, M.; Kim, S. J.; Han, B. S.; Kim, S. H.; Kim, H. O.; Sheen, Y. Y.; Jeong, J. The impact of size on tissue distribution and elimination by single intravenous injection of silica nanoparticles. *Toxicol. Lett.* **2009**, *189*, 177–183.
- (41) Dufort, S.; Sancey, L.; Coll, J.-L. Physico-chemical parameters that govern nanoparticles fate also dictate rules for their molecular evolution. *Adv. Drug Delivery Rev.* **2012**, *64* (2), 179–89.
- (42) Osseo-Asare, K.; Arriagada, F. J. Growth Kinetics of Nanosize Silica in a Nonionic Water-in-Oil Microemulsion: A Reverse Micellar Pseudophase Reaction Model. *J. Colloid Interface Sci.* **1999**, *218*, 68–76.
- (43) Arriagada, F. J.; Osseo-Asare, K. Controlled hydrolysis of tetrathoxysilane in a nonionic water-in-oil microemulsion: A statistical model of silica nucleation. *Colloids Surf. A: Physicochem. Eng. Aspects* **1999**, *154*, 311–326.
- (44) Arriagada, F. J.; Osseo-Asare, K. Synthesis of Nanosize Silica in a Nonionic Water-in-Oil Microemulsion: Effects of the Water/Surfactant Molar Ratio and Ammonia Concentration. *J. Colloid Interface Sci.* **1999**, *211*, 210–220.
- (45) Jin, Y.; Lohstreter, S.; Pierce, D. T.; Parisien, J.; Wu, M.; Hall, C., III; Zhao, J. X. Silica nanoparticles with continuously tunable sizes: Synthesis and size effects on cellular contrast imaging. *Chem. Mater.* **2008**, *20* (13), 4411–4419.
- (46) Jin, J.-M.; Parbhakar, K.; Dao, L. H. Model for water-in oil microemulsions: Surfactant effects. *Phys. Rev. E* **1997**, *55*, 721–726.
- (47) Chand, C.-L.; Fogler, S. Controlled Formation of Silica Particles from Tetraethyl Orthosilicate in Nonionic Water-in-Oil Microemulsions. *Langmuir* **2007**, *13*, 3295–3307.
- (48) Park, S. K.; Kim, K. D.; Kim, H. T. Preparation of silica nanoparticles: Determination of the optimal synthesis conditions for small and uniform particles. *Colloids Surf. A: Physicochem. Eng. Aspects* **2002**, *197*, 7–17.
- (49) Yao, L.; Xu, G.; Dou, W.; Bai, Y. The control of size and morphology of nanosized silica in Triton X-100 based reverse micelle. *Colloids Surf. A* **2008**, *316*, 8–14.
- (50) Zhao, M.; Zheng, L.; Bai, X.; Li, N.; Yu, L. Fabrication of silica nanoparticles and hollow spheres using ionic liquid microemulsion droplets as templates. *Colloids Surf. A: Physicochem. Eng. Aspects* **2009**, *346*, 229–236.
- (51) Pinho, S. L. C.; Faneca, H.; Geraldes, C. F. G. C.; Delville, M.-H.; Carlos, L. D.; Rocha, J. Lanthanide-DTPA grafted silica nanoparticles as bimodal-imaging contrast agents. *Biomaterials* **2012**, *33*, 925–935.
- (52) Frangioni, J. V. In vivo near-infrared fluorescence imaging. *Curr. Opin. Chem. Biol.* **2003**, *7*, 626–634.
- (53) Sevcik-Muraca, E. M.; Houston, J. P.; Gurfinkel, M. Fluorescence-enhanced, near infrared diagnostic imaging with contrast agents. *Curr. Opin. Chem. Biol.* **2002**, *6*, 642–650.
- (54) Gerardi, R. D.; Barnett, N. W.; Lewis, S. W. Analytical applications of tris(2,20-bipyridyl)ruthenium(III) as a chemiluminescent reagent. *Anal. Chim. Acta* **1999**, *378*, 1–41.
- (55) Helm, L. Relaxivity in paramagnetic systems: Theory and mechanisms. *Prog. Nucl. Magn. Reson. Spectrosc.* **2006**, *49*, 45–64.
- (56) Sharma, P.; Brown, S. C.; Walter, G.; Santra, S.; Scott, E.; Ichikawa, H.; Fukumori, Y.; Moudgil, B. M. Gd nanoparticulates: From magnetic resonance imaging to neutron capture therapy. *Adv. Powder Technol.* **2007**, *18* (6), 663–698.